




Investigation of cardiopulmonary bypass parameters on embolus transport in a patient-specific aorta

Nafis M. Arefin¹ · Bryan C. Good¹ 

Received: 12 March 2024 / Accepted: 5 June 2024

© The Author(s), under exclusive licence to Springer-Verlag GmbH Germany, part of Springer Nature 2024

Abstract

Neurological complexities resulting from surgery requiring cardiopulmonary bypass (CPB) remain a major concern, encompassing a spectrum of complications including thromboembolic stroke and various cognitive impairments. Surgical manipulation during CPB is considered the primary cause of these neurological complications. This study addresses the overall lack of knowledge concerning CPB hemodynamics within the aorta, employing a combined experimental-computational modeling approach, featuring computational fluid dynamics simulations validated with an in vitro CPB flow loop under steady conditions. Parametric studies were systematically performed, varying parameters associated with CPB techniques (pump flow rate and hemodiluted blood viscosity) and properties related to formed emboli (size and density). This represents the first comprehensive investigation into the individual and combined effects of these factors. Our findings reveal critical insights into the operating conditions of CPB, indicating a positive correlation between pump flow rate and emboli transport into the aortic branches, potentially increasing the risk of stroke. It was also found that larger emboli were more often transported into the aortic branches at higher pump flow rates, while smaller emboli preferred lower flow rates. Further, as blood is commonly diluted during CPB to decrease its viscosity, more emboli were found to enter the aortic branches with greater hemodilution. The combined effects of these parameters are captured using the non-dimensional Stokes number, which was found to positively correlate with emboli transport into the aortic branches. These findings contribute to our understanding of embolic stroke risk factors during CPB and shed light on the complex interplay between CPB parameters.

Keywords Computational fluid dynamics · Cardiopulmonary bypass · Lagrangian particle tracking · Embolus transport · Stroke · OpenFOAM

1 Introduction

The development and application of cardiopulmonary bypass (CPB) to permit open heart surgery is considered one of the greatest advances in twentieth century medicine. In 1933, John Gibbon proposed the theory and model of extracorporeal circulation and demonstrated that utilizing a machine to function as a heart would allow for open-heart surgery while maintaining perfusion to all other organs (Gibbon 1937). Today, approximately 500,000 surgeries using CPB are performed annually in the USA (Tsao et al. 2023). Current CPB protocols include interventions, such as the reduction in core body temperature and hemodilution, that have an

impact on blood viscosity. The deliberate lowering of core body temperature during CPB reduces the body's oxygen demand, while concurrently elevating blood viscosity. To counteract this, hemodilution is routinely administered, but it has been found to increase cerebral blood flow (Jonas et al. 2003; Sakamoto et al. 2004), potentially increasing the risk of micro-embolic load to the brain (Holsworth et al. 2013). The optimal extent of hemodilution to be applied remains unclear, with certain studies indicating that a lower hematocrit can have adverse impacts on both neurocognitive and renal functions (Karkouti et al. 2005; Ranucci et al. 2015). Hence, there is a notable absence of experimental and computational studies investigating the impact of blood viscosity variations on CPB hemodynamics.

With recent advancements in computational fluid dynamics (CFD), it is now possible to conduct complex numerical simulations of the cardiovascular system. Notably, some researchers have studied hemodynamics in the aortic arch

✉ Bryan C. Good
bgood6@utk.edu

¹ Department of Mechanical, Aerospace, and Biomedical Engineering, University of Tennessee, Knoxville, TN, USA

during CPB but have omitted experimental validation from their analyses (Tokuda et al. 2008). Similarly, analyses of CPB blood pumps have been performed to evaluate shear stresses on blood but without experimental validation (Fiore et al. 2009; Formato et al. 2019; Mulholland et al. 2005; Zhou et al. 2014). Emboli generated during CPB can be transported through the bloodstream to various organs, including the brain, liver, and kidneys (Hampton et al. 1989; Karkouti et al. 2005; Tirilomis et al. 2009). Malone et al. simulated embolus transport through an aortic arch model under atrial fibrillation conditions (Malone et al. 2019a, b), while McGah (2019) performed two-way coupled embolus transport simulations in a carotid artery bifurcation. Khodae et al. (2016) developed a computational model to predict embolus transport in the cerebrovascular system with mixed Eulerian–Lagrangian techniques, however, it was shown to be computationally expensive and impractical for CPB geometries and time scales. Aycock et al. (2014) made significant progress by devising a computationally efficient coupled CFD-discrete element model, enabling large-scale simulations in patient-specific models. Few research groups, however, have also attempted to observe embolus transport in the cerebrovascular system. Fabbri et al. (2014) conducted computational studies to observe flow dynamics through an anatomical Circle of Willis (CoW) model, while Mukherjee et al. simulated embolus distribution in CoW models (Mukherjee et al. 2018; Mukherjee et al. 2016a, b). Their studies exclusively simulated emboli with diameters ranging from 100 to 1000 μm and utilized a one-way coupled model with no momentum transfer between particles and blood. Additionally, most computational models have relied on simplified boundary conditions, which can not address the changes in aortic resistances and compliances under elevated perfusion pressures and CPB flow rates.

Despite the previous CFD research in this field, no studies have investigated the effect of patient blood viscosity on CPB hemodynamics, which is critical for understanding patient-to-patient heterogeneity in postoperative outcomes.

Although some research groups have used mock circulatory flow loops (MCFLs) to replicate flow dynamics within blood pumps or cerebrovascular systems, none have collectively merged them into a single research model with embolus transport and varying flow parameters to determine their individual effects. Furthermore, while several studies have attempted to model embolus transport and distribution in the aorta, none have done so with physiologically accurate emboli, anatomies, CPB hemodynamic properties, or validated their results with experimental studies (Mukherjee et al. 2018; Mukherjee et al. 2016a, b; Mukherjee et al. 2016a, b). To address these shortcomings, an improved experimental MCFL will be developed and used to observe emboli distribution in the aortic arch under varying pump flow rates, fluid viscosities, and embolus sizes and densities. This experimental dataset will then be used to validate computational simulations of emboli transport in the aorta during CPB, with the goal of minimizing potential neurological complications during cardiovascular surgery.

2 Methods

2.1 Silicone aorta model development

A silicone model of an aortic arch consisting of the ascending aorta (AA), brachiocephalic artery (BCA), left common carotid artery (LCCA), left subclavian artery (LSCA), and descending artery (DA) was developed. A patient-specific aortic arch geometry of a 26-year-old healthy male (Fig. 1a) was first obtained from the Vascular Model Repository (Wilson et al. 2013), an open-source database of cardiovascular models. A CAD model of the geometry was then created with the addition of a CPB outlet cannula anastomosed to the ascending aorta (Fig. 1b). This model was then 3D printed out of polyvinyl alcohol (PVA), a soft and biodegradable polymer, using an Ultimaker S3 printer (Fig. 1c). An outer box was also 3D printed out of polylactic acid

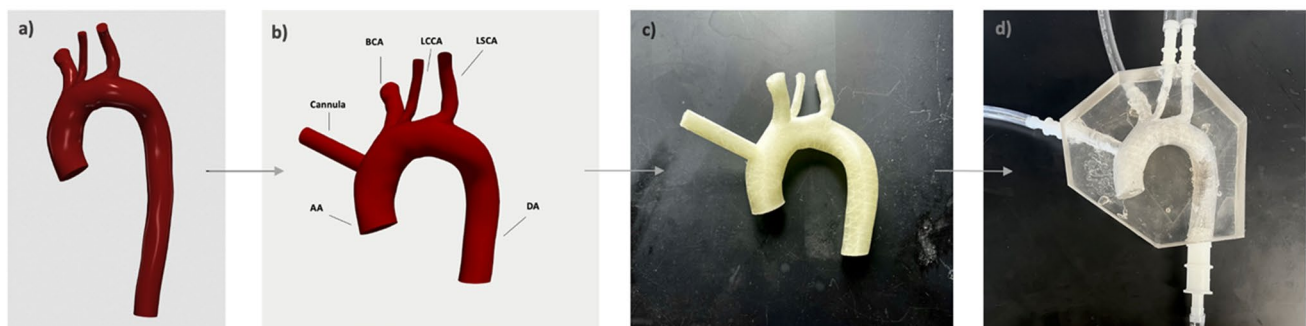


Fig. 1 **a** Patient-specific aorta from the vascular model repository (Wilson et al. 2013). **b** Developed CAD model with an anastomosed CPB cannula. **c** 3D-printed PVA model and **d** final silicone model incorporated into the MCFL

(PLA) (not shown) that allowed for the PVA aorta to be placed inside and subsequently filled with SYLGARD-184, a two-component silicone-based elastomeric kit. Following a 3-day solidification period, the model was submerged in hot water for another 2 days to completely dissolve away the PVA, leaving behind a cavity representing the fluid domain of the aortic model. Finally, tube connectors were fixed to each of the model's inlet and outlets to allow for incorporation into a mock circulatory flow loop (MCFL) (Fig. 1d).

2.2 CPB mock circulatory flow loop

The MCFL was developed using the silicone aorta model as shown in Fig. 2. The MCFL also included a Sorin Stockert Roller Pump (10-10-00 CAPS Module 10H), 3/8-inch and 1/4-inch inner diameter PVC tubing with connectors, a fluid reservoir, tubing resistance clamps for flow rate control, and ultrasonic flow probes and flow meter (Transonic) to monitor total pump and aortic branch flow rates. Resistance was applied at each outlet of the aorta using clamps to achieve flow distributions of 15.7, 7.8, 7.8, and 68.7% into the brachiocephalic artery (BCA), left common carotid artery (LCCA), left subclavian artery (LSA), and descending aorta (DA), respectively, following patient data from Benim et al. (2011).

Fluid exiting the aorta model through the DA travels to the lower body, eliminating the likelihood of embolic

delivery to the brain and causing strokes. However, there is an increased risk of emboli lodging in the kidneys, leading to various renal complications (Khilji and Khan 2004). The percentage of the total flow rate through the BCA is approximately twice that of both the LCCA and LSCA. The brachiocephalic trunk further branches into the right subclavian artery, supplying blood to the right arm, and the right carotid artery, supplying blood to the brain and the right side of the head and neck. Likewise, the LSCA supplies blood to the left arm and the back of the brain, while the LCCA supplies blood to the brain and the left side of the head and neck (Chandran 1993). Thus, emboli exiting from any of the branches in the aortic arch pose a threat of traveling into the cerebral vasculature and causing a stroke.

2.3 Blood and embolus analogs

To cover the range of hemodiluted blood viscosities observed during CPB, five distinct blood analog solutions were prepared by carefully mixing water and glycerin at specific volume ratios (Volk and Kähler 2018): (1) 88:12 for $\mu \approx 1.5$ cP, (2) 80:20 for $\mu \approx 2$ cP, (3) 74:26 for $\mu \approx 2.5$ cP, (4) 70:30 for $\mu \approx 3$ cP, and (5) 67:33 for $\mu = 3.5$ cP. Furthermore, to represent emboli formed in the CPB system, spherical nylon beads of two different diameters (2.4 mm (1/16 inch) and 1.6 mm (3/32 inch)) were used in the experimental setup. In each experimental trial, a single bead was

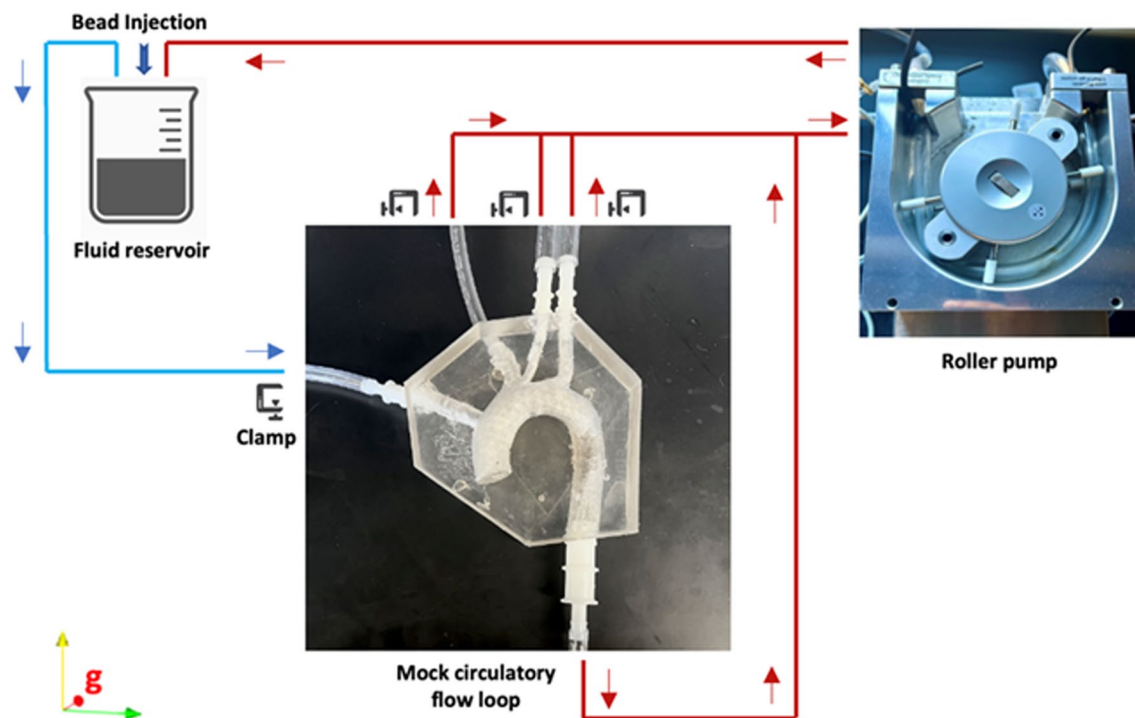


Fig. 2 The developed MCFL for studying embolus transport during CPB

injected into the flow loop and its trajectory and exit through one of the aortic branches or descending aorta were noted. To calculate the percent distribution of each emboli type, the total number of beads exiting through each branch were divided by the total number of beads injected into the system via the CPB cannula.

2.4 Experimental sample size

Sample size calculations were performed to confirm the validity and reliability of the experimental study. Following established guidelines set by Krejcie and Morgan (1970), the sample size (n) was determined using Eq. 1:

$$n = \frac{z^2 \hat{p}(1 - \hat{p})}{\epsilon^2} \quad (1)$$

where ‘ z ’ is the z -score associated with the chosen confidence level, ‘ ϵ ’ is the desired margin of error, and ‘ \hat{p} ’ is the estimated sample population proportion. The sample size ‘ n ’ then represents the minimum number of trials needed to estimate the true population proportion with the required margin of error and confidence level and thus determines the minimum number of trials required to maintain statistical power. The sample population proportion ‘ \hat{p} ’ can often be determined by prior surveys or pilot studies (Daniel and Cross 2018). In this specific case, a pilot study was first conducted to observe particle transport in the MCFL and revealed that approximately 10% of particles exited through BCA, 5% through each of the BCCA and LSCA, and 80% through the DA. Using a predicted value of 80% transport through the DA as our population proportion to provide the highest necessary sample size for experimental validation, we also assumed an infinite population size, a margin of error of 5%, and a 90% confidence level (z -score of 1.645) and found the necessary sample size to be approximately 173.2. Therefore, at least 174 trials were needed for each experimental case to ensure the reliability of our results.

2.5 CFD model development

A CAD model of a patient-specific aorta was developed for the computational simulations (Fig. 1b). The model, an aortic arch anatomy of a 26-year-old male with no cardiovascular complications, was obtained from the Vascular Model Repository (Wilson et al. 2013). A cylindrical CPB outlet cannula was attached to the model using Blender, an open-source software for editing and rendering 3D geometries, to facilitate the injection of emboli into the aorta. Blender was also used to remove any unnecessary portions of the aortic anatomy and to define the model’s inlet and outlet boundary patches for CFD.

OpenFOAM (OpenCFD, Ltd.), an open-source C++ computational continuum mechanics library, was used to solve the Reynolds-averaged Navier Stokes (RANS) equations under steady flow conditions. To accurately capture turbulent flow exiting CPB cannula (peak Reynolds numbers of approximately 3860 for 3 L per minute (LPM) flow rate and 6440 for 5 LPM flow rate), the k - ω shear-stress transport (k - ω SST) (Menter 1994), a two-equation eddy-viscosity model, was employed. This turbulence model was preferred because of its robust efficacy in handling adverse pressure gradients and separated flows and its demonstrated capability to address multi-regime flows (Zhang and Kleinstreuer 2003). Large eddy simulation (LES) turbulence modeling, using the Smagorinsky sub grid-scale model, was also performed on the two extreme Reynolds number cases and all emboli transport results were within 0.1 to 4% of the RANS model results. Based on these small observed differences, and the significantly higher computational costs associated with higher LES mesh resolutions and smaller time scales, the k - ω SST RANS model was employed for all presented CFD simulations.

The governing equations were solved using a previously validated OpenFOAM solver (*pisoFoam*), which uses the finite volume method alongside the pressure implicit with the splitting of the operator (PISO) algorithm to compute the pressure and velocity fields. The linear solvers used a generalized geometric/algebraic multi-grid (GAMG) solver for pressure and a preconditioned bi-conjugate gradient (PBICG) solver for velocity. To ensure stability and precision, dynamic time-step control was implemented to maintain a Courant number below 1, with the residuals of all variables converging to 10^{-6} at each time step. Flow simulations were first run for 2.5 s for each case to ensure they reached a steady state, followed by Lagrangian particle tracking simulations that were conducted for 30 s of simulation time to allow all injected emboli to exit the aortic model. Post-processing and visualization of the simulation results were performed in ParaView.

To conduct a systemic grid sensitivity study and ensure that the numerical simulations remained independent of the mesh they are solved on, we generated three high-quality unstructured meshes of the aortic arch model utilizing OpenFOAM’s ‘snappyHexMesh’ utility. This consisted of coarse (~ 700,000 cells), medium (~ 1,200,000 cells), and fine (~ 1,800,000 cells) meshes with predominantly hexahedral interior cells and three wall layers added to each mesh. Two different CPB cases were simulated to determine the sensitivity of emboli distribution to the mesh. For Case A, a pump flow rate of 3 LPM was simulated with 3.5 cP blood and large emboli (2.4 mm diameter) with a density of 1092.4 kg/m³. For Case B, the same pump flow rate and blood viscosity were used but with small emboli (1.6 mm diameter) with a higher density of 1134 kg/m³.

2.6 Boundary conditions

CFD boundary conditions were defined to align with the corresponding in vitro experiments. Pressure boundary conditions were prescribed at the outlets of the three aortic arch branches and the descending aorta to achieve physiologically accurate flow distribution (Eq. 2):

$$p = RQ + p_0 \quad (2)$$

where ' p ' is pressure, ' R ' is a resistance constant, ' Q ' is flow rate, and ' p_0 ' is the mean arterial pressure. Iterative CFD simulations were carried out to determine the correct resistance coefficient (R) at each outlet for all blood viscosity and flow rate cases, resulting in ten distinct sets of resistance coefficients that matched the experimental flow distributions of 15.7, 7.8, 7.8, and 68.7% through the BCA, LCCA, LSA, and DA, respectively (Benim et al. 2011). Additionally, zero velocity gradient boundary conditions were applied at all outlets, and no-slip velocity boundary conditions on all walls.

2.7 Lagrangian particle tracking

Lagrangian particle tracking (LPT) was used to investigate emboli distribution through the aortic arch. LPT is a volumetric flow measurement technique that allows for the tracking of a large number of tracer particles over extended time periods, even in highly turbulent scenarios (Yeoh and Tu 2019). In this study, the method for evaluating particle transport was performed using the validated LPT solver '*particleFoam*' implemented within *OpenFOAM*. The *OpenFOAM* Lagrangian directory '*cloudProperties*' allows for the introduction of particles into the flow using several built-in injection models and tracks their positions according to specified forces. In this study, each parcel was treated as an individual embolus, and a manual injection model that enables the injection of particles with specified diameters and positions within the fluid domain was applied. In total, 1000 particles were injected through the cannula inlet in each simulation to ensure high enough

numbers of particles would exit through the aortic branches with overall low percentage distributions. The particles were injected with the same velocity as fluid entering the model in the CPB cannula and particle collisions were disabled, assuming that only a single embolus would be injected from the CPB circuit into the aorta at a time. Particles were defined to rebound upon contact with the aortic wall using the '*patchInteractionModel*' tool within the '*cloudProperties*' directory. Additionally, Young's modulus and Poisson's ratio of the wall were defined to replicate the characteristics of a real aorta wall (Giannakoulas et al., 2005) using the '*wallModel*' tool within '*cloudProperties*'.

As shown in Fig. 3, the particles were tracked until they exited through one of the aortic outlets. In phase (i), the injection of emboli into the aorta model is observed, and they begin exiting through the outlets in phase (ii) until nearly all have left the fluid domain by phase (iv).

The motion of particles in fluids was described in a Lagrangian manner by solving a set of ordinary differential equations along their trajectories using Euler first-order integration schemes. The objective was to calculate the changes in particle location and the linear and angular components of the particle velocity. Also, the relevant forces acting on each particle needed to be accounted for. In this study, the particles were assumed to be spheres representing emboli generated in the CPB circuit. The forces considered to have a major contribution to overall particle dynamics were sphere drag, gravity, and the local pressure gradient. The differential equations for calculating each particle location (x_p) and linear (u_p) and angular (ω_p) velocities are described by Eqs. 3, 4, and 5, respectively:

$$\frac{dx_p}{dt} = u_p \quad (3)$$

$$I_p \frac{d\omega_p}{dt} = T \quad (4)$$

$$m_p \frac{du_p}{dt} = \sum F_i \quad (5)$$

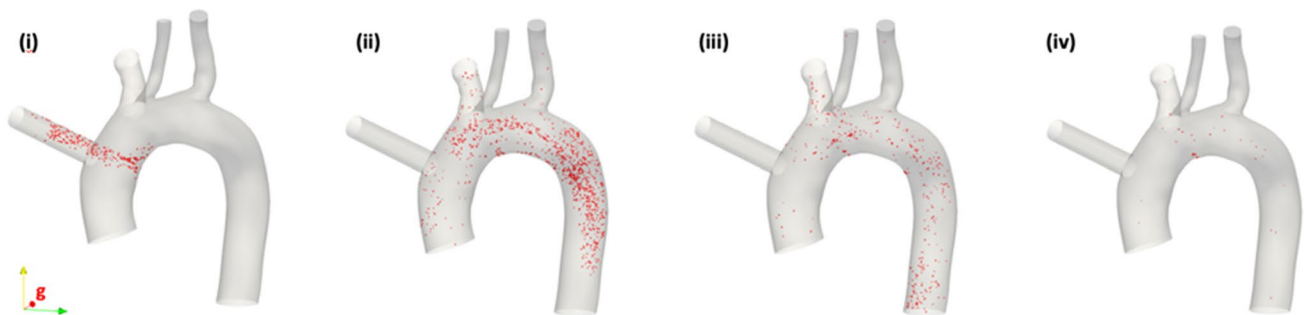


Fig. 3 Example of computational emboli transport modeling through the aortic arch over time

where ' I_p ' is the moment of inertia for a sphere, ' T ' is the torque acting on a rotating particle due to the surrounding fluid, ' m_p ' is the particle mass found from Eq. 6, and ' F_i ' is the sum of the forces acting on each particle found from Eq. 7:

$$m_p = \frac{\pi_p d_p^3}{6} \quad (6)$$

$$F_i = F_D + F_g + F_p \quad (7)$$

In Eq. 6, ' ρ_p ' is the particle density and ' d_p ' is the particle diameter. The drag force on a spherical particle (F_D) is calculated using Eq. 8:

$$F_D = m_p \frac{18\mu C_D \text{Re}}{\rho_p d_p^2} (u - u_p) \quad (8)$$

the gravity force (F_g) is calculated using Eq. 9:

$$F_g = m_p g \left(1 + \frac{\rho}{\rho_p} \right) \quad (9)$$

and the force from the local pressure gradient (F_p) is calculated from Eq. 10:

$$F_p = \frac{1}{6} d_p^3 \nabla P \quad (10)$$

In this set of particle force equations (Eqs. 8–10), ' μ ' is the fluid viscosity, ' C_D ' is the particle drag coefficient, ' Re ' is the Reynolds number, ' u ' is the fluid velocity, ' g ' is the gravitational acceleration constant, ' ρ ' is the fluid density, and ' ∇P ' is the local pressure gradient.

2.8 Varying CPB and emboli parameters

2.8.1 CPB parameters

To match the experimental blood analogs used in the in vitro study, and to cover the range of clinically relevant hemodiluted blood viscosity, five distinct fluids were simulated with viscosities of 1.5, 2, 2.5, 3, and 3.5 cP. CPB pump flow rate, measured in liters per minute (LPM), is clinically calculated as the product of an individual patient's body surface area (BSA) and a constant of 2.2–2.4 (Jw et al. 1955; Starr 1959). BSA, determined using the Du Bois formula (Eq. 11), is derived from the patient's height and weight, under the assumption that each square meter of body mass carries a consistent metabolic rate (Bois 1989).

$$\text{BSA} [\text{m}^2] = \text{Weight} [\text{kg}]^{0.425} \times \text{Height} [\text{cm}]^{0.725} \times 0.007184 \quad (11)$$

In our study, we used this formula to determine BSA values and subsequently the corresponding pump flow rates, for two distinct patient groups at the extremes of the BSA spectrum. Ultimately, we chose flow rates of 3 and 5 LPM to represent patients with lower and higher BSAs, respectively.

2.8.2 Emboli parameters

We aimed to introduce emboli of diverse sizes and densities into our study to observe the overall effect on their transport in correlation with other parameters during CPB. Notably, prior research established that smaller-sized emboli, less than 0.2 mm, travel proportionally to the flow (Chung et al. 2010), prompting us to exclude microemboli from our study. Additionally, it has been found that aortic emboli can possess diameters ranging from 0.3 to 2.9 mm (Barbut et al. 1997). Addressing this size criterion, we chose to employ two distinct emboli sizes, 2.4 mm (3/32 inch) and 1.6 mm (1/16 inch) in both the experimental and computational studies. We also performed simulations with three distinct emboli densities. Given that the densities of emboli are inherently equal to or greater than that of the blood they are formed from, we chose one emboli density to match the density of the hemodiluted blood in which they were suspended. The remaining two emboli densities were chosen to be 1092 kg/m³ (equivalent to the density of whole blood with a viscosity of 3.5 cP) and 1134 kg/m³ (matching the nylon beads used in the experimental study).

2.8.3 Stokes number and emboli transport

The behavior of a particle suspended in a fluid flow is characterized by a dimensionless number known as the Stokes number. The Stokes number (St) (Eq. 12) is the ratio of the particle's momentum response time to the flow-field time scale (Birzer et al. 2012):

$$\text{St} = \frac{\rho_p D_p^2 u_0}{18\mu_0 D_0} \quad (12)$$

where ρ_p is the particle density, D_p is the particle diameter, u_0 is the fluid velocity, μ_0 is the fluid dynamic viscosity, and D_0 is the characteristic length scale of flow, typically its diameter. For $\text{St} > 1$, particles tend to detach from the fluid flow streamlines due to the dominance of their inertia over the viscous forces. Conversely, when $\text{St} < 1$, particles will closely follow the fluid streamlines as their inertia becomes negligible compared to the viscous forces of the fluid (Tropea et al. 2007). For our set of 60 CFD-LPT computational simulations with varying emboli densities and diameters and fluid velocities and viscosities, the calculated Stokes numbers ranged between 1.96 and 17.09.

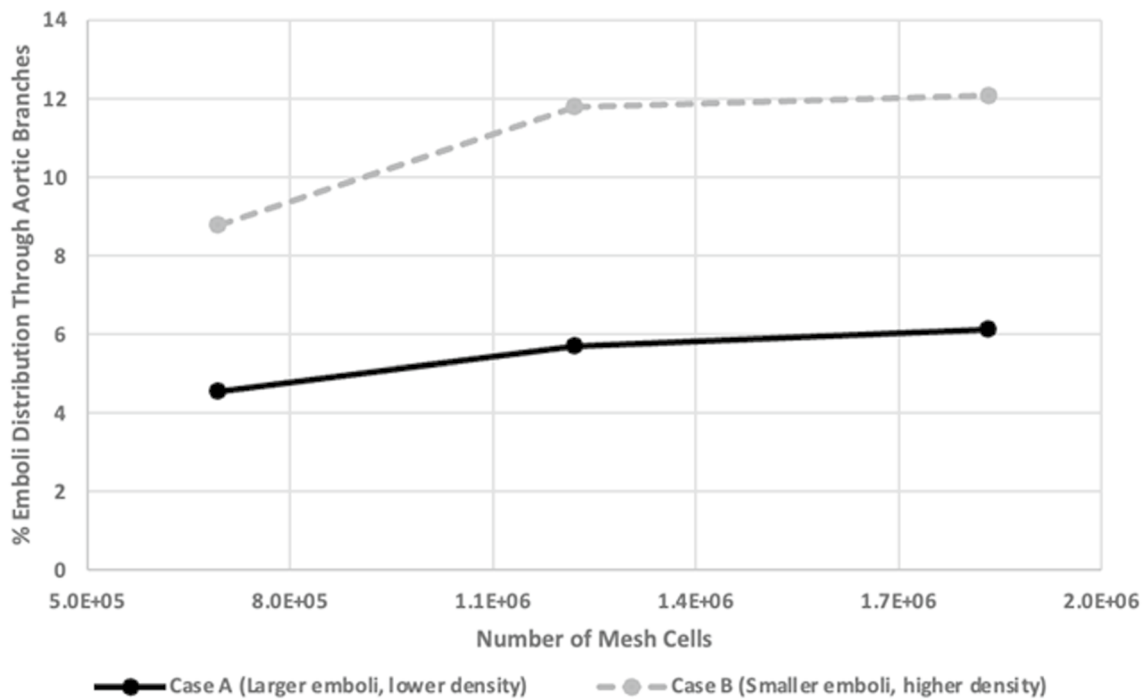


Fig. 4 Grid convergence study of emboli transport

3 Results

3.1 Grid convergence

As mentioned previously in Sect. 2.5, two CPB cases were simulated to determine the influence of grid refinement on resultant predictions of emboli transport. Case A featured large emboli (2.4 mm) with a lower density (1092.4 kg/m³), while Case B featured small emboli (1.6 mm) with a higher density (1134 kg/m³). A 20% difference in emboli exiting through the aortic branches was observed for Case A between the coarse and medium meshes, whereas only a 7% difference was found between the medium and fine meshes. Similarly, for Case B, a 25.6% increase in particles exiting through the aortic branches was found between the coarse and medium meshes, while only a 2.5% increase was observed between the medium and fine meshes (Fig. 4).

To quantitatively estimate the numerical uncertainty, the grid convergence index (GCI) was calculated using generalized Richardson extrapolation (Richardson and Gaunt 1927). Following the guidelines of Roache (1994), a factor of safety of 1.25 was used for unstructured meshes to provide an upper limit on the relative discretization error. In this study, for Case A, the GCIs for the medium and fine meshes were calculated to be 15.1 and 5.3%, respectively, and for Case B, they were calculated to be 3.5 and 0.3%, respectively. Even though a slightly higher GCI was found for Case A, this resulted in only a small amount of uncertainty in the actual

emboli distribution magnitudes. For example, the percentages of emboli entering the aortic branches for the Case A medium and fine meshes were 5.7 and 6.1%, respectively. Based on these results, the medium computational mesh was determined to be sufficiently refined and was used for all subsequent CFD simulations.

3.2 Experimental Emboli Transport

The experimental distribution of both large (L) and small (S) beads throughout the aortic branches and DA are shown in Fig. 5 for all blood analog viscosities. Overall, between 10–21% of beads exited through one of the aortic arch branches and between 79–90% of beads exited through the DA. It was observed that the percentage of small beads (1.6 mm) exiting through the aortic branches was greater than that of the large beads (2.4 mm) for all fluids except for 1.5 cP, where the opposite trend was observed. Similarly, the percentage of large beads exiting through the DA was higher than that of the small beads for all fluids except for 1.5 cP. Additionally, a 5% margin of error (ϵ) was assumed for all experimentally averaged data based on initial calculations (Eq. 1) to determine the experimental sample size (n) in Section 2.4.

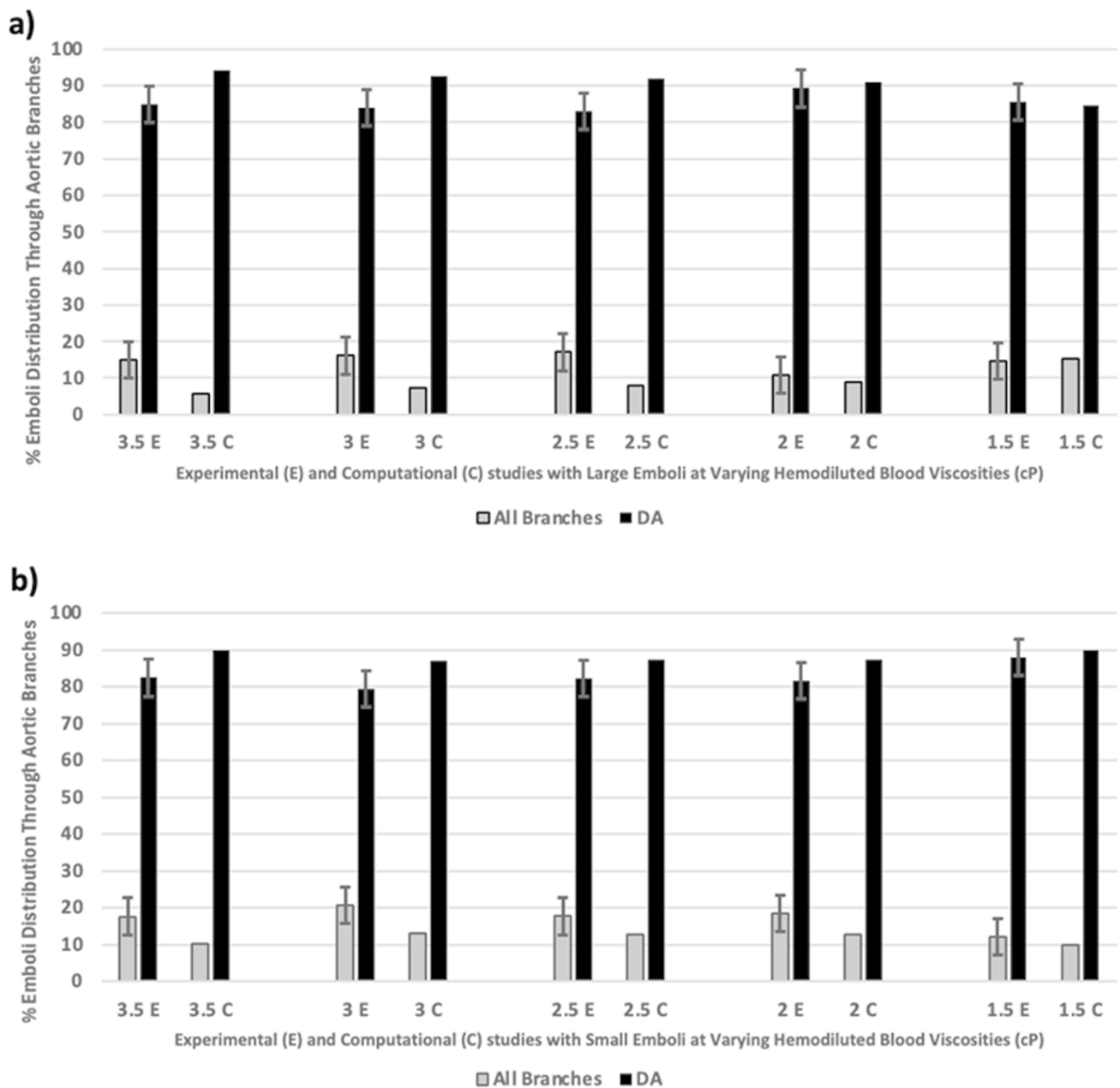


Fig. 5 Comparison of experimental (E) and computational (C) embolus transport distribution into the aortic branches at a 3 LPM pump flow rate for a) large and b) small emboli

3.3 Computational model validation

The computational results mirrored the trends observed in emboli distribution in the in vitro experiments for both large (Fig. 5a) and small (Fig. 5b) emboli studies. It was found that the percentage of small emboli (1.6 mm) entering the aortic branches was also greater than that of the large emboli (2.4 mm) for all fluid viscosities ranging from 3.5 to 2 cP, but lower for the 1.5 cP fluid. In terms of the large emboli (Fig. 5a), a 5.6% difference in emboli exiting through the

aortic branches was predicted with the computational simulation, while for small emboli, this difference was 6.2% (Fig. 5b).

It was observed for the higher viscosity fluid cases (3.5 and 3 cP), however, that the computational model slightly underpredicted the amount of emboli delivered to the aortic branches. This contrasts with the more hemodiluted cases (2.5, 2, and 1.5 cP) where there was excellent agreement between the experimental and computational results (emboli transport predictions within the 5% experimental margins

of error). We believe this discrepancy to be a result of the lower, and not fully turbulent, Reynolds numbers of the CPB cannula inlet jet in the 3.5 and 3 cP cases (approximately 1990 and 2250, respectively). Our CFD simulations incorporated RANS turbulence modeling, which assumes fully turbulent flow, and could explain why the experimental hemodynamics in the transitional flow regimes for these two cases may not be accurately captured. Apart from this, consistent trends were observed in both the experimental and computational emboli trajectories, including a shift in distribution for the 1.5 cP fluid and similar distribution percentages across all five blood viscosity cases, providing confidence in the simulated results and the overall computational modeling framework.

3.4 Aortic flow during CPB

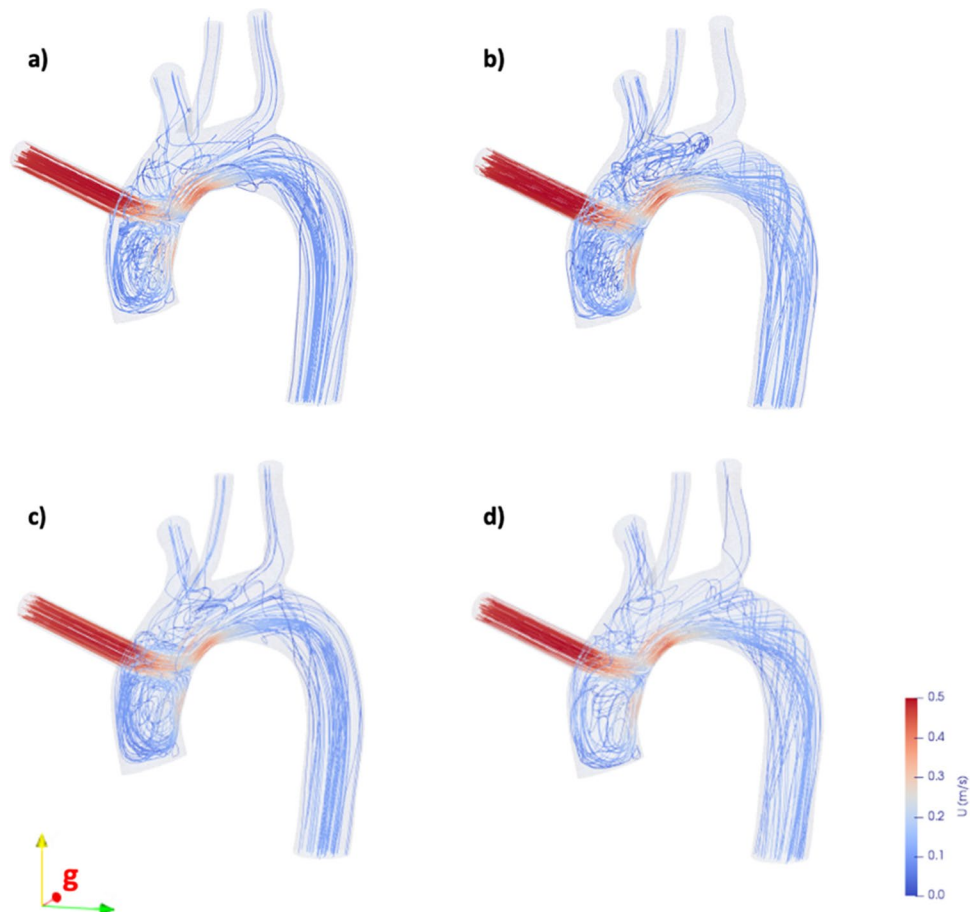
Fluid streamlines during different CPB operating conditions are shown in Fig. 6 to help identify variations in the velocity fields, which correspondingly influence emboli transport in the aorta. In Fig. 6a and b, fluid streamlines during CPB with a 1.5 cP blood viscosity are shown for pump flow rates of 3 and 5 LPM, respectively. Similarly, Fig. 6c and d highlight the fluid streamlines for a 3.5 cP blood viscosity at 3 and 5 LPM

5 LPM pump flow rates, respectively. It can be observed that at a higher 5 LPM flow rate (Fig. 6b and d), the fluid exiting the CPB cannula is considerably more chaotic due to the development of turbulent conditions ($Re \approx 6440$). It was also observed that in the lower blood viscosity (1.5 cP) cases (Fig. 6a and c), the fluid streamlines more closely followed the inner wall of curvature in the aortic arch, while the higher viscosity (3.5 cP) cases displayed more flow along the distal wall of the descending aorta.

3.5 Effect of CPB pump flow rate and hemodiluted blood viscosity

As previously discussed, simulations were performed at 3 and 5 LPM flow rates with varying blood viscosities (3.5 to 1.5 cP). In Fig. 7, the percentages of emboli exiting through the aortic branches during CPB are shown, combining the results of both large and small emboli sizes. For all five blood viscosities, a marked increase in emboli exiting through the aortic branches is observed at the higher 5 LPM pump flow rate, in comparison to the 3 LPM condition. For different cases, we observed a substantial rise in emboli transport, from 12 to 42%, during the transition from the 3 to the 5 LPM pump flow rate. The results also indicate

Fig. 6 Fluid streamlines through the aorta during CPB at **a** 1.5 cP blood at 3 LPM, **b** 1.5 cP blood at 5 LPM, **c** 3.5 cP blood at 3 LPM, and **d** 3.5 cP blood at 5 LPM



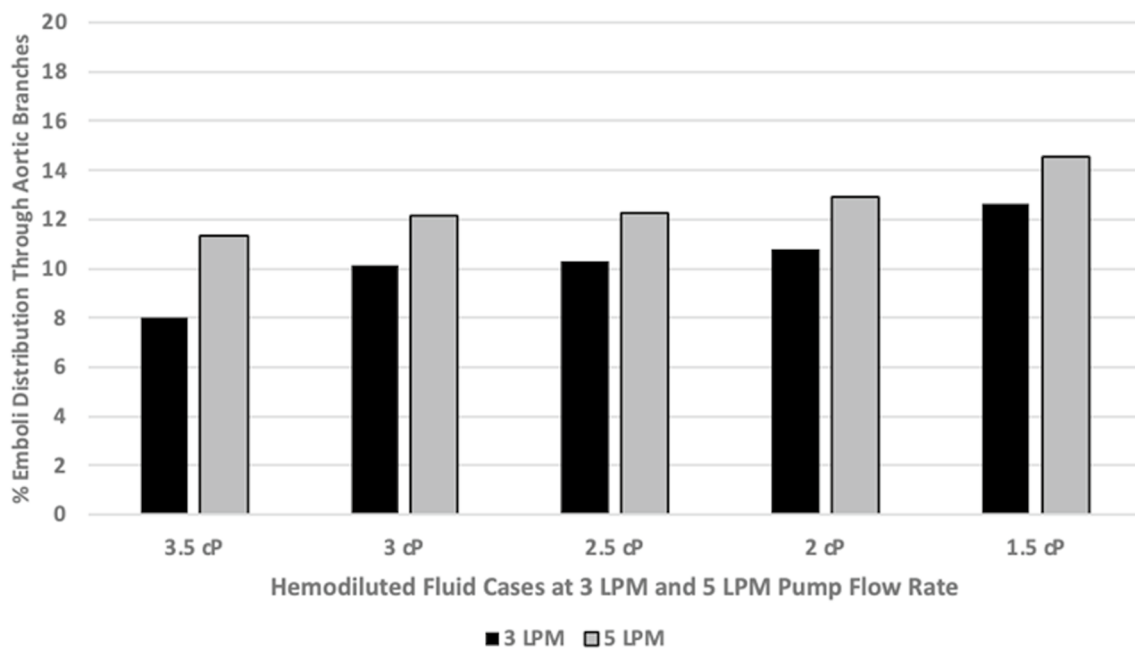


Fig. 7 Computational emboli transport into the aortic branches for varying CPB pump flow rates and hemodiluted blood viscosities

a direct correlation between decreased blood viscosity and the transport of emboli into the aortic branches. Specifically, the probability of an embolus exiting into an aortic branch is approximately $1.5\times$ higher with 1.5 cP hemodiluted blood compared to 3.5 cP non-hemodiluted blood.

3.6 Effect of embolus density

The relationship between emboli density and hemodiluted blood viscosity is illustrated in Fig. 8. The dataset includes three distinct emboli density cases: (1) emboli density matches that of its corresponding hemodiluted blood, (2) emboli density matches that of non-hemodiluted 3.5 cP blood (1092 kg/m^3), and (3) emboli density matches that of the nylon experimental beads (1134 kg/m^3). It was determined that for the combined large and small emboli dataset (Fig. 8a), as the density of the emboli decreased, they were more likely to exit through one of the aortic branches. Specifically, the emboli with the highest density (1134 kg/m^3) were 7% less likely to be delivered to the aortic branches. However, in Fig. 8b, when only the small emboli are analyzed, there are different trends with regard to emboli density and their distribution depending on the fluid viscosity. This difference in behaviors can be explained by Stokes law (Eq. 12), where particle diameter in the numerator is squared and has a greater impact on the Stokes number compared to particle density and fluid viscosity. For the smaller diameter emboli, however, this has less of an overall impact on the Stokes number and the role of varying particle density and fluid viscosity becomes more pronounced.

3.7 Effect of embolus size

The relationship between emboli size and pump flow rate is illustrated in Fig. 9a, which combines emboli transport results from all hemodiluted blood viscosities and emboli densities. It was found that large emboli have a 27% higher likelihood of entering the aortic branches at higher pump flow rates, while small emboli demonstrate a 40% higher likelihood at lower pump flow rates. Additionally, Fig. 9b shows the percentage of both emboli sizes exiting through the aortic branches at the single 5 LPM flow condition. The results show that as blood viscosity decreases, there is an increase in the percentage of large emboli exiting through the aortic branches (90% increase from 3.5 to 1.5 cP blood viscosity). Conversely, for small emboli, the exit percentages remained relatively unchanged, showing that their transport is less impacted by hemodilution.

3.8 Effect of stokes number

The percentage distribution of emboli into the aortic branches were compared as a function of the Stokes number (Eq. 12). In Fig. 10, ten 5 LPM flow rate cases are highlighted with emboli of both sizes and all fluid viscosities included. The figure showcases the critical role that Stokes number, which is a function of emboli size, emboli density, fluid velocity, and fluid viscosity, has on determining the trajectory of emboli in the aortic arch. For the 5 LPM CPB flow rate cases analyzed, there is a near linear

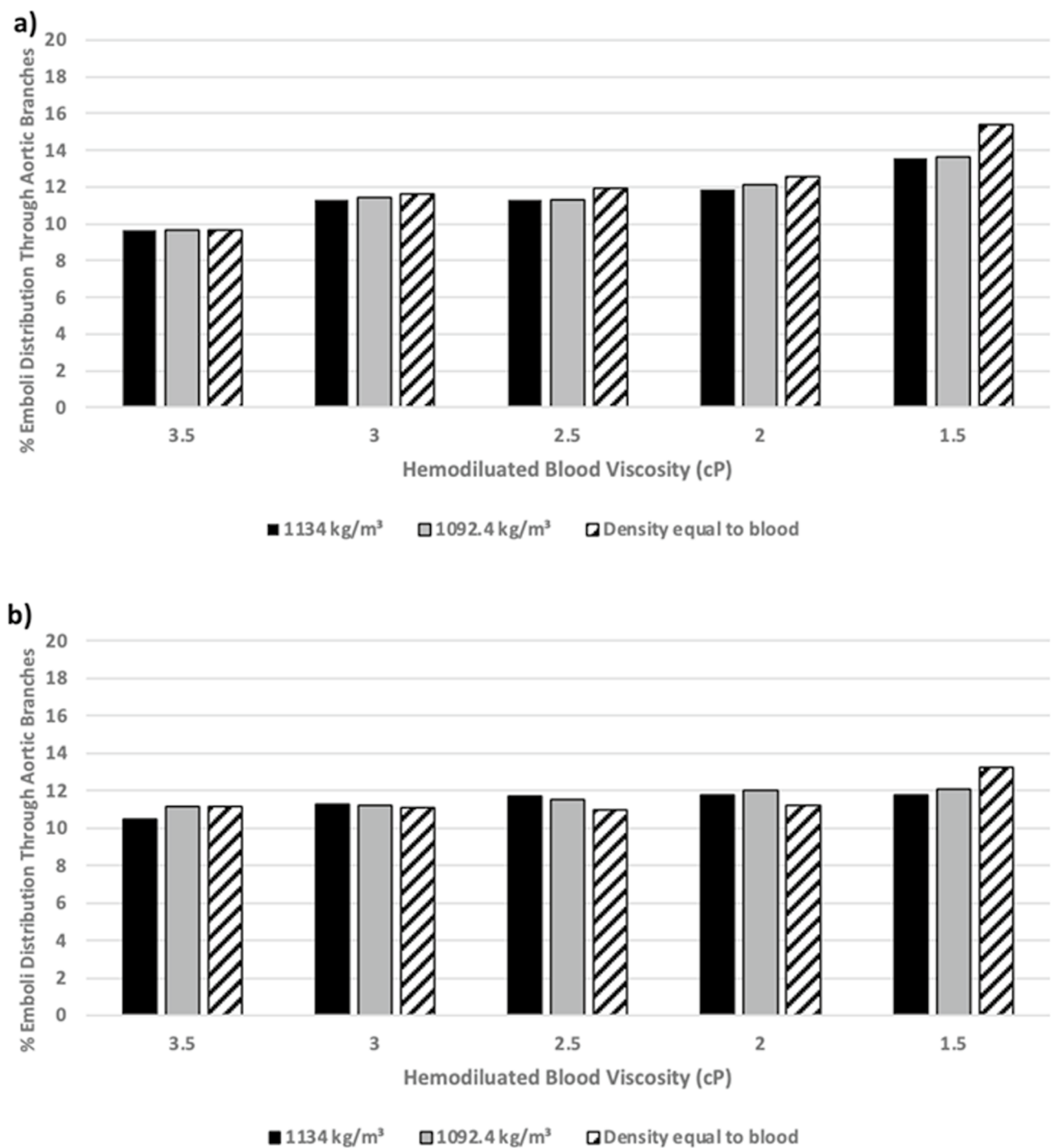


Fig. 8 Computational emboli transport into the aortic branches with varying emboli densities, shown for a) combined emboli sizes (1.6 and 2.4 mm), and b) smaller emboli size only (1.6 mm)

relationship between the percentage of emboli that enter the branches of the aortic arch and the Stokes number with the highest Stokes number cases resulting in the highest distribution into the aortic branches.

4 Discussion

The present study provides critical insights into the intricate interplay of different parameters during CPB. The

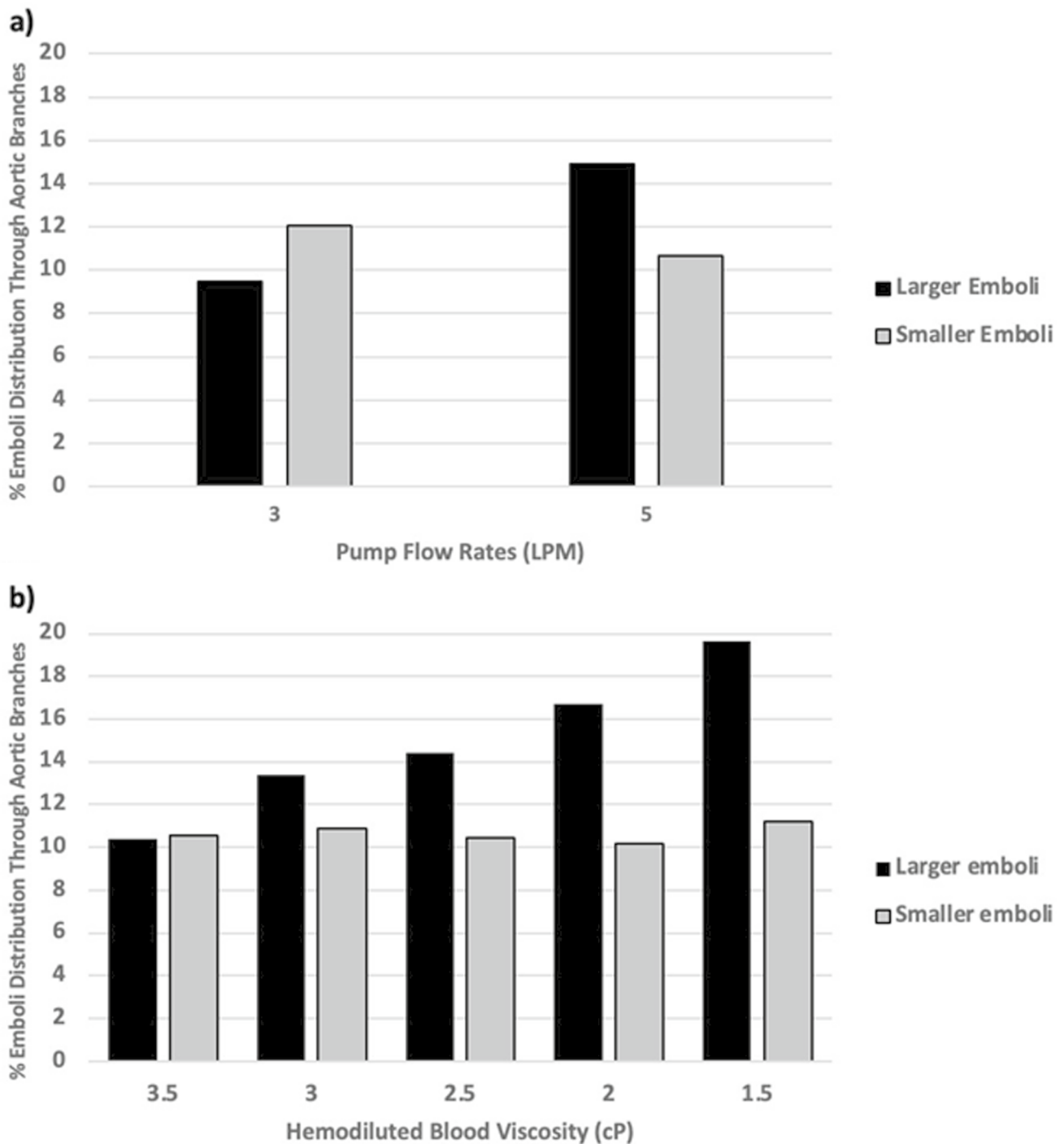


Fig. 9 Comparison of computational emboli transport into the aortic branches for **a** 3 and 5 LPM pump flow rates and for **b** varying blood viscosities at the 5 LPM flow rate condition, highlighting the influence of embolus size on both CPB parameters

investigated CPB and emboli parameters included pump flow rate, hemodiluted blood viscosity, embolus size, and embolus density. The in vitro model developed in this study represented a CPB roller pump and circuit anastomosed to a patient aorta model to simulate realistic CPB conditions and was used to validate computational

simulations predicting emboli distribution to the aortic branches. Blood flow through the aorta during CPB displays complex behaviors (Fig. 6) and understanding the nature of this complexity and its effect on emboli transport stands as a crucial challenge.

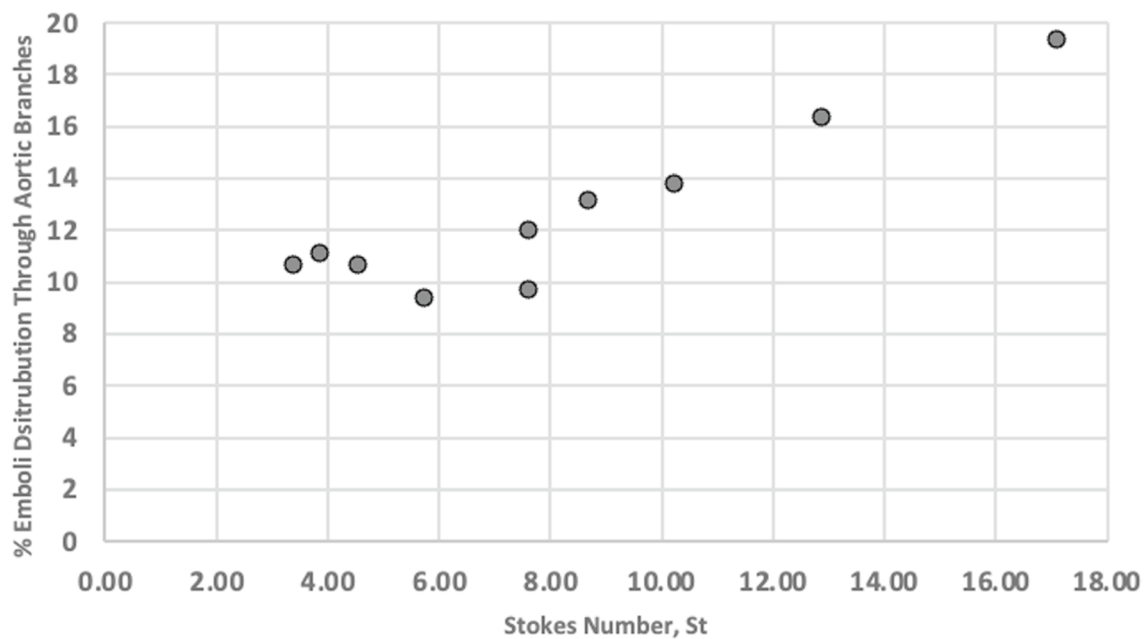


Fig. 10 Computational emboli transport into the aortic branches as a function of Stokes number, highlighting ten of the 5 LPM flow rate cases including all emboli sizes and blood viscosities

Our simulations showed that as blood viscosity decreased, a higher number of emboli exited through the aortic branches (Fig. 7). Specifically, the probability of emboli exiting through the aortic branches in 1.5 cP hemodiluted blood viscosity was approximately $1.5 \times$ greater than that in 3.5 cP whole blood. As blood undergoes hemodilution and hematocrit levels decrease, the fluid becomes less viscous due to the reduction in RBC concentration. This can also lead to a decrease in frictional forces between the blood and vasculature. Thus, the emboli find it easier to deviate from the fluid streamlines and navigate toward the slow-moving near-wall regions within the aorta, facilitating their tendency to exit through the aortic branches.

Also, it was observed that a greater number of emboli exit through the aortic branches at higher pump flow rates (42% increase from 3 to 5 LPM) and consequently, they tended to exit through the descending aorta at lower pump flow rates (Fig. 7). This behavior could be attributed to the turbulent nature of the flow entering the ascending aorta at higher pump flow rates. As the central regions of the aortic arch experience faster flows, while the near-wall regions are characterized by slow flow, emboli that follow the fluid streamlines will migrate toward the center of the vessel and will be more likely to exit through the descending aorta (directing approximately 68.7% of the total flow). As a result of more turbulence at higher pump flow rates, emboli could more easily deviate from their streamlines and preferentially exit through the aortic branches. This finding highlights the

critical role that pump flow rate has in influencing the distribution of particles.

Also, from Stokes law (Eq. 12), it is evident that an increase in pump flow rate (resulting in increased fluid velocity, u_0) is proportional to the Stokes number while an increase in fluid viscosity, μ_0 , is inversely proportional to the Stokes number. For instance, a CPB case with smaller emboli, a pump flow rate of 3 LPM, and a blood viscosity of 3.5 cP will result in a Stokes number of only 2.03. By increasing the pump flow rate to 5 LPM and decreasing the blood viscosity to 1.5 cP, the Stokes number will then increase to 7.60. The higher the Stokes number increases above $St = 1$, the less influence the carrier fluid has on changing particle motion. This suggests that at higher pump flow rates and lower viscosities, more emboli enter the aortic branches, which was expectedly observed in our study. This relationship between Stokes number and emboli trajectories into the aortic branches is further shown in Fig. 10, where a near linear relationship is demonstrated as Stokes number increases for the 5 LPM CPB flow rate cases encompassing both emboli sizes and all fluid viscosities.

We also observed that irrespective of their sizes and flow rates, emboli with lower density are more likely to exit through an aortic branch compared to the DA (Fig. 8a). This behavior can partially be explained by buoyancy forces, which will have a greater effect on emboli with lower density applied by the blood. This results in them rising within the flow and deviating from the flow streamlines, preferentially directing them toward the aortic branches. Emboli with

higher density experience lower buoyant forces and tend to sink in the flow, directing them to the flow streamline and out through the DA. Conversely, in Fig. 8b when only the smaller emboli are analyzed, a decrease in density leads to a lower probability of emboli exiting through one of the aortic branches in viscosity cases of 3.5, 3, and 2.5 cP. However, this trend was not consistent for the lower viscosity cases (2 and 1.5 cP). This behavior can also be explained by Stokes law (Eq. 12) where particle diameter in the numerator is squared and has a greater impact on the Stokes number compared to particle density. For the smaller diameter emboli, however, this has less of an overall impact on the Stokes number and the role of varying fluid viscosity becomes more pronounced.

Our results also showed that, in the case of 5 LPM CPB flow, large emboli were more likely to exit through the aortic branches as blood viscosity decreased, while the behavior of small emboli remained relatively unchanged (Fig. 9b). This tendency can be attributed to both their reduced mass and momentum and also the lower drag forces experienced by the smaller emboli, allowing them to align with the primary fluid streamlines independent of changes in hematocrit levels. Large emboli, on the other hand, experience greater drag forces due to their size and are also harder to accelerate due to the combined effects of their size and density (i.e., mass and momentum). These factors will collectively reduce their likelihood to change direction through the aortic arch, directing them toward the outer wall and increasing their tendency to exit through the aortic branches.

Our findings align with previous studies of particle transport during CPB. Computational studies by Fabbri et al. (2014) and Abolfazli et al. (2014) observed that variations in emboli size and density are associated with higher emboli transport through branches with higher flow splits, a correlation consistent with our own findings. Additionally, our results correspond with the computational study by Ho et al. (2023), which also reported that a higher pump flow rate leads to a greater number of emboli exiting through the aortic branches. For emboli originating at different locations, Mukherjee et al. (2016a, b) similarly identified notable size-dependent trends in the transport of emboli to the Circle of Willis. Furthermore, the observed flow patterns in the aortic arch during our investigation broadly corresponded to those shown computationally by Numata et al. (2016).

The present study has certain limitations that should be taken into consideration in future research. Firstly, both the experimental and computational emboli were modeled as rigid perfect spheres. In reality, emboli exhibit irregular shapes, and their viscoelastic mechanical properties may prove critical, particularly when simulating larger-sized emboli and their interactions with the vessel walls. Furthermore, the CFD simulations did not account for the pulsatile nature of blood flow and vessel wall movement. However, we assumed the

ascending aorta to be clamped during surgery and that inflow from the CPB circuit into the ascending aorta is quasi-steady. Although a $k-\omega$ SST RANS model was utilized to capture the turbulent behavior of blood exiting the CPB inlet cannula, and preliminary results showed minimal differences in predicted emboli trajectories compared to LES simulations, LES models should still be investigated in the future as they have been shown to capture complex turbulent flows more accurately. However, their significantly greater computational costs, as a result of higher resolution meshes and smaller time scales, must also be weighed when performing a large number of simulations using patient-specific cardiovascular anatomies. Additionally, emboli trajectories were only observed in the aortic arch and not the cerebral vasculature. Therefore, our simulations do not directly predict whether an embolus will travel into the CoW and cause a stroke. However, as mentioned in Sect. 2.2, estimations regarding the number of emboli that can reach the brain can be made based on the downstream anatomy of each branch. Also in this study, we incorporated one patient anatomy and one cannula orientation. Our future investigations will address these limitations and include varied anatomical and geometrical parameters to provide a more comprehensive characterization of CPB flow and emboli transport.

The findings from this study lead us to suggest optimal operating conditions during CPB to minimize the risk of embolic stroke. It can be recommended that the CPB pump flow rate should not be maintained at the upper limit based on the patient's BSA, and that the patient's blood should not be excessively hemodiluted if possible. The findings from our combined experimental-computational approach hold significant implications for understanding stroke biomechanics and treatment planning during CPB. The potential applications of these findings will be useful for reducing the risk of stroke and complications associated with CPB, thereby enhancing the overall safety of cardiovascular surgery.

Author contributions N.A. performed all the experimental and computational studies, prepared the results, wrote the original draft, and reviewed the final manuscript. B.G. conceptualized and supervised the study and edited and reviewed the final manuscript.

Funding No funds, grants, or other support was received.

Declarations

Conflict of interest The authors have no relevant financial or non-financial interests to disclose.

References

- Abolfazli E, Fatouraei N, Vahidi B (2014) Dynamics of motion of a clot through an arterial bifurcation: a finite element analysis. *Fluid Dyn Res* 46(5):055505

- Aycock KI, Campbell RL, Manning KB, Sastry SP, Shontz SM, Lynch FC, Craven BA (2014) A computational method for predicting inferior vena cava filter performance on a patient-specific basis. *J Biomech Eng* 136(8):081003
- Barbut D, Yao F-SF, Lo Y-W, Silverman R, Hager DN, Trifiletti RR, Gold JP (1997) Determination of size of aortic emboli and embolic load during coronary artery bypass grafting. *Ann Thorac Surg* 63(5):1262–1265
- Benim A, Nahavandi A, Assmann A, Schubert D, Feindt P, Suh S (2011) Simulation of blood flow in human aorta with emphasis on outlet boundary conditions. *Appl Math Model* 35(7):3175–3188
- Birzer CH, Kalt PA, Nathan GJ (2012) The influences of particle mass loading on mean and instantaneous particle distributions in precessing jet flows. *Int J Multiph Flow* 41:13–22
- Bois D (1989) A formula to estimate the approximate surface area if height and weight be known. *Nutrition* 5:303
- Chandran KB (1993) Flow dynamics in the human aorta. *J Biomech Eng* 115(4B):611–616. <https://doi.org/10.1115/1.2895548>
- Chung EM, Hague JP, Chanrion M-A, Ramnarine KV, Katsogridakis E, Evans DH (2010) Embolus trajectory through a physical replica of the major cerebral arteries. *Stroke* 41(4):647–652
- Daniel WW, Cross CL (2018) *Biostatistics: a foundation for analysis in the health sciences*. Wiley
- Fabbri D, Long Q, Das S, Pinelli M (2014) Computational modelling of emboli travel trajectories in cerebral arteries: influence of micro-embolic particle size and density. *Biomech Model Mechanobiol* 13(2):289–302
- Fiore GB, Morbiducci U, Ponzini R, Redaelli A (2009) Bubble tracking through computational fluid dynamics in arterial line filters for cardiopulmonary bypass. *ASAIO J* 55(5):438–444
- Formato G, Romano R, Formato A, Sorvari J, Koironen T, Pellegrino A, Vilecco F (2019) Fluid–structure interaction modeling applied to peristaltic pump flow simulations. *Machines* 7(3):50
- Giannakoulas G, Giannoglou G, Soulis J, Farmakis T, Papadopoulos S, Parcharidis G, Louridas G (2005) A computational model to predict aortic wall stresses in patients with systolic arterial hypertension. *Med Hypotheses* 65(6):1191–1195
- Gibbon JH (1937) Artificial maintenance of circulation during experimental occlusion of pulmonary artery. *Arch Surg* 34(6):1105–1131
- Hampton WW, Townsend MC, Schirmer WJ, Haybron DM, Fry DE (1989) Effective hepatic blood flow during cardiopulmonary bypass. *Arch Surg* 124(4):458–459
- Ho R, McDonald C, Pauls JP, Li Z (2023) Effect of aortic cannulation depth on air emboli transport during cardiopulmonary bypass: A computational study. *Perfusion* 38(5):993–1001
- Holsworth R, Shechterle L, St Cyr J, Sloop G (2013) Importance of monitoring blood viscosity during cardiopulmonary bypass. *Perfusion* 28(1):91
- Jonas RA, Wypij D, Roth SJ, Bellinger DC, Visconti KJ, Du Plessis AJ, Goodkin H, Laussen PC, Farrell DM, Bartlett J (2003) The influence of hemodilution on outcome after hypothermic cardiopulmonary bypass: results of a randomized trial in infants. *J Thorac Cardiovasc Surg* 126(6):1765–1774
- Jw K, Jw D, DE D, HG H, EH W (1955) Intracardiac surgery with the aid of a mechanical pump-oxygenator system (gibbon type): report of eight cases. *Proceedings of the staff meetings*. Mayo Clinic
- Karkouti K, Beattie W, Wijeyesundera D, Rao V, Chan C, Dattilo K, Djaiani G, Ivanov J, Karski J, David T (2005) Hemodilution during cardiopulmonary bypass is an independent risk factor for acute renal failure in adult cardiac surgery. *J Thorac Cardiovasc Surg* 129(2):391–400
- Khilji SA, Khan AH (2004) Acute renal failure after cardiopulmonary bypass surgery. *J Ayub Med Coll* 16(3):25–28
- Khodae F, Vahidi B, Fatouraee N (2016) Analysis of mechanical parameters on the thromboembolism using a patient-specific computational model. *Biomech Model Mechanobiol* 15:1295–1305
- Krejcie RV, Morgan DW (1970) Determining sample size for research activities. *Educ Psychol Measur* 30(3):607–610
- Malone F, McCarthy E, Delassus P, Buhk J, Fiehler J, Morris L (2019a) Embolus analog trajectory paths under physiological flowrates through patient-specific aortic arch models. *J Biomech Eng* 141(10):101007
- Malone F, McCarthy E, Delassus P, Buhk J-H, Fiehler J, Morris L (2019b) Investigation of the hemodynamics influencing emboli trajectories through a patient-specific aortic arch model. *Stroke* 50(6):1531–1538
- McGah PM (2019) Embolus transport simulations with fully resolved particle surfaces. *Cardiovasc Eng Technol* 10(4):648–659
- Menter FR (1994) Two-equation eddy-viscosity turbulence models for engineering applications. *AIAA J* 32(8):1598–1605
- Mukherjee D, Jani ND, Selvaganesan K, Weng CL, Shadden SC (2016a) Computational assessment of the relation between embolism source and embolus distribution to the circle of Willis for improved understanding of stroke etiology. *J Biomech Eng* 138(8):081008
- Mukherjee D, Padilla J, Shadden SC (2016b) Numerical investigation of fluid–particle interactions for embolic stroke. *Theoret Comput Fluid Dyn* 30:23–39
- Mukherjee D, Jani ND, Narvid J, Shadden SC (2018) The role of circle of Willis anatomy variations in cardio-embolic stroke: a patient-specific simulation based study. *Ann Biomed Eng* 46:1128–1145
- Mulholland JW, Shelton J, Luo X (2005) Blood flow and damage by the roller pumps during cardiopulmonary bypass. *J Fluids Struct* 20(1):129–140
- Numata S, Itatani K, Kanda K, Doi K, Yamazaki S, Morimoto K, Manabe K, Ikemoto K, Yaku H (2016) Blood flow analysis of the aortic arch using computational fluid dynamics. *Eur J Cardiothorac Surg* 49(6):1578–1585
- Ranucci M, Aloisio T, Carboni G, Ballotta A, Pistuddi V, Menicanti L, Frigiola A, Surgical, & Group, C. O. R (2015) Acute kidney injury and hemodilution during cardiopulmonary bypass: a changing scenario. *Ann Thorac Surg* 100(1):95–100
- Richardson LF, Gaunt JA (1927) VIII The deferred approach to the limit. *Philos Trans Royal Soc London Ser A Contain Papers Math Phys Character* 226(636646):299–361
- Roache PJ (1994) Perspective: a method for uniform reporting of grid refinement studies. *J Fluids Eng* 116(3):405–413. <https://doi.org/10.1115/1.2910291>
- Sakamoto T, Nollert GD, Zurakowski D, Soul J, Duebener LF, Sperling J, Nagashima M, Taylor G, Jonas RA (2004) Hemodilution elevates cerebral blood flow and oxygen metabolism during cardiopulmonary bypass in piglets. *Ann Thorac Surg* 77(5):1656–1663
- Starr A (1959) Oxygen consumption during cardiopulmonary bypass. *J Thorac Cardiovasc Surg* 38(1):46–56
- Tirilomis T, Tempes T, Waldmann-Beushausen R, Ballat C, Bensch M, Schoendube FA (2009) Histological changes in neonatal kidneys after cardiopulmonary bypass and deep hypothermic circulatory arrest. *Thorac Cardiovasc Surg* 57(01):7–9
- Tokuda Y, Song M-H, Ueda Y, Usui A, Akita T, Yoneyama S, Maruyama S (2008) Three-dimensional numerical simulation of blood flow in the aortic arch during cardiopulmonary bypass. *Eur J Cardiothorac Surg* 33(2):164–167
- Tropea C, Yarin AL, Foss JF (eds) (2007) *Springer handbook of experimental fluid mechanics*. Springer, Berlin, Heidelberg. <https://doi.org/10.1007/978-3-540-30299-5>
- Tsao CW, Aday AW, Almarzooq ZI, Anderson CA, Arora P, Avery CL, Baker-Smith CM, Beaton AZ, Boehme AK, Buxton AE (2023) Heart disease and stroke statistics—2023 update: a report from the American Heart Association. *Circulation* 147(8):e93–e621

- Volk A, Kähler CJ (2018) Density model for aqueous glycerol solutions. *Exp Fluids* 59(5):75
- Wilson NM, Ortiz AK, Johnson AB (2013) The vascular model repository: a public resource of medical imaging data and blood flow simulation results. *J Med Devices* 7(4):040923
- Yeoh GH, Tu J (2019) *Computational techniques for multiphase flows*. Butterworth-Heinemann
- Zhang Z, Kleinstreuer C (2003) Low-Reynolds-number turbulent flows in locally constricted conduits: a comparison study. *AIAA J* 41(5):831–840
- Zhou X, Liang XM, Zhao G, Su Y, Wang Y (2014) A new computational fluid dynamics method for in-depth investigation of flow dynamics in roller pump systems. *Artif Organs* 38(7):E106–E117

Publisher's Note Springer Nature remains neutral with regard to jurisdictional claims in published maps and institutional affiliations.

Springer Nature or its licensor (e.g. a society or other partner) holds exclusive rights to this article under a publishing agreement with the author(s) or other rightsholder(s); author self-archiving of the accepted manuscript version of this article is solely governed by the terms of such publishing agreement and applicable law.